

## FINDING THE FIRST COSMIC EXPLOSIONS. III. PULSATONAL PAIR-INSTABILITY SUPERNOVAE

DANIEL J. WHALEN<sup>1,2</sup>, JOSEPH SMIDT<sup>1</sup>, WESLEY EVEN<sup>3</sup>, S. E. WOOSLEY<sup>4</sup>, ALEXANDER HEGER<sup>5</sup>, MASSIMO STIAVELLI<sup>6</sup> AND CHRIS L. FRYER<sup>3</sup>

*Draft version March 16, 2021*

### ABSTRACT

Population III supernovae have been the focus of growing attention because of their potential to directly probe the properties of the first stars, particularly the most energetic events that can be seen at the edge of the observable universe. But until now pulsational pair-instability supernovae, in which explosive thermonuclear burning in massive stars fails to unbind them but can eject their outer layers into space, have been overlooked as cosmic beacons at the earliest redshifts. These shells can later collide and, like Type II<sub>n</sub> supernovae, produce superluminous events in the UV at high redshifts that could be detected in the near infrared today. We present numerical simulations of a  $110 M_{\odot}$  pulsational pair-instability explosion done with the Los Alamos radiation hydrodynamics code RAGE. We find that collisions between consecutive pulsations are visible in the near infrared out to  $z \sim 15 - 20$  and can probe the earliest stellar populations at cosmic dawn.

*Subject headings:* early universe – galaxies: high-redshift – galaxies: quasars: general – stars: early-type – supernovae: general – radiative transfer – hydrodynamics – black hole physics – cosmology:theory

### 1. INTRODUCTION

Population III (Pop III) stars ended the cosmic Dark Ages and began to reionize (Whalen et al. 2004; Kitayama et al. 2004; Alvarez et al. 2006; Abel et al. 2007; Wise & Abel 2008) and chemically enrich (Mackey et al. 2003; Smith & Sigurdsson 2007; Smith et al. 2009; Chiaki et al. 2013; Ritter et al. 2012; Safranek-Shrader et al. 2013) the early intergalactic medium (IGM). They also populated early galaxies (Johnson et al. 2008; Greif et al. 2008; Johnson et al. 2009; Greif et al. 2010; Jeon et al. 2012; Pawlik et al. 2011; Wise et al. 2012; Pawlik et al. 2013) and might be the origin of supermassive black holes (Bromm & Loeb 2003; Johnson & Bromm 2007; Djorgovski et al. 2008; Milosavljević et al. 2009; Alvarez et al. 2009; Lippai et al. 2009; Tanaka & Haiman 2009; Park & Ricotti 2011, 2012; Johnson et al. 2012; Whalen & Fryer 2012; Agarwal et al. 2012; Johnson et al. 2013c; Park & Ricotti 2013; Latif et al. 2013a,b; Schleicher et al. 2013; Choi et al. 2013; Reisswig et al. 2013; Volonteri 2012).

Unfortunately, little is known for certain of the properties of the first stars. Individual Pop III stars will not be visible to next-generation instruments such as the *James Webb Space Telescope (JWST)*; Gardner et al. 2006) or the Thirty-Meter Telescope (TMT; but see

Rydberg et al. 2013, about detecting the H II regions of the first stars). Attempts to constrain the Pop III initial mass function (IMF) from stellar archaeology are problematic because of the many processes can enrich ancient, dim stars with metals over cosmic time (e.g., Cayrel et al. 2004; Beers & Christlieb 2005; Frebel et al. 2005; Lai et al. 2008; Joggerst et al. 2010; Caffau et al. 2012). Simulations are far from being able to model the formation of Pop III stars at  $z \sim 20$  from first principles (e.g., Abel et al. 2002; Bromm et al. 2002; Nakamura & Umemura 2001; Turk et al. 2009; Stacy et al. 2010; Clark et al. 2011; Hosokawa et al. 2011; Smith et al. 2011; Greif et al. 2011, 2012; Stacy et al. 2012; Hosokawa et al. 2012; Susa 2013; Hirano et al. 2013) and therefore do not yet predict their final masses or numbers in a given halo (for recent reviews, see Whalen 2012; Glover 2013).

Several groups have now turned to Pop III supernovae (SNe) as potential probes of the primordial IMF because they can be observed at high redshifts and their masses can be deduced from their light curves. The first studies focused on pair-instability (PI) SNe, the extremely energetic thermonuclear explosions of  $140 - 260 M_{\odot}$  stars (Heger & Woosley 2002; Scannapieco et al. 2005; Whalen et al. 2008b; Gal-Yam et al. 2009; Cooke et al. 2012; Joggerst & Whalen 2011; Whalen et al. 2013d). They found that Pop III PI SNe could be detected at  $z \gtrsim 20$  by *JWST* and the TMT and at  $z \sim 10 - 20$  in all-sky near infrared (NIR) surveys by the Wide-Field Infrared Survey Telescope (WFIRST) and the Wide-Field Imaging Surveyor for High-Redshift (WISH) (Fryer et al. 2010; Kasen et al. 2011; Whalen et al. 2013a,e; Pan et al. 2012; Hummel et al. 2012; Dessart et al. 2013; de Souza et al. 2013). Other simulations have now shown that Pop III core-collapse (CC) SNe can be seen out to  $z \sim 10 - 15$  with *JWST* (Whalen et al. 2013f) and that Type II<sub>n</sub> SNe and supermassive thermonuclear explosions (Whalen et al. 2013c;

<sup>1</sup> T-2, Los Alamos National Laboratory, Los Alamos, NM 87545, USA

<sup>2</sup> Zentrum für Astronomie, Institut für Theoretische Astrophysik, Universität Heidelberg, Albert-Ueberle-Str. 2, 69120 Heidelberg, Germany

<sup>3</sup> CCS-2, Los Alamos National Laboratory, Los Alamos, NM 87545, USA

<sup>4</sup> Department of Astronomy and Astrophysics, UCSC, Santa Cruz, CA 95064, USA

<sup>5</sup> Monash Centre for Astrophysics, Monash University, Victoria, 3800, Australia

<sup>6</sup> Space Telescope Science Institute, 3700 San Martin Drive, Baltimore, MD 21218, USA

Johnson et al. 2013b; Whalen et al. 2013h,g) are visible at  $z \sim 10 - 20$ .

Until now, pulsational pair-instability (PPI) SNe, in which the PI fails to unbind the star and instead heaves off its outer layers in a series of violent ejections, have been overlooked as cosmic beacons at high redshifts. These episodes vary in energy and mass but the first ejection is usually the most massive one, with later pulsations ejecting less massive shells at higher velocities. The later shells can overtake the first, producing collisions that are very luminous in the UV. Three PPI SN candidates have been found at low redshifts, SN 1000-1216 at  $z = 3.9$  (Cooke et al. 2012), SN2009ip (Margutti et al. 2013; Smith et al. 2013), and perhaps SN 2006oz at  $z = 0.376$  (Leloudas et al. 2012). This mechanism has also been invoked to explain superluminous SNe such as SN 2006gy (Smith & McCray 2007; Woosley et al. 2007). At early epochs, the large UV fluxes of PPI SNe would be redshifted into the NIR today and could rival those of PI SNe. Indeed, other types of shell-collision explosions are now known to be visible at  $z \sim 10 - 20$  (Tominaga et al. 2011; Moriya et al. 2013; Tanaka et al. 2012; Whalen et al. 2013b; Tanaka et al. 2013). PPI SNe may be more numerous than PI SNe in the early universe, depending on the primordial IMF.

We have now modeled Pop III PPI SNe and their spectra and light curves with the Los Alamos RAGE and SPECTRUM codes. In Section 2 we review the PPI SN mechanism and discuss our numerical methods and explosion models in Section 3. Pair pulsations and their collisions are examined in Section 4. In Section 5, we calculate NIR light curves for the collision in the observer frame, and we conclude in Section 6.

## 2. PPI SN EXPLOSION MECHANISM

It is generally known that Pop III stars from  $140 - 260 M_{\odot}$  die as PI SNe, but they can actually encounter the PI at  $\sim 100 M_{\odot}$  (and at masses as low as  $85 M_{\odot}$  if they are rotating; Chatzopoulos & Wheeler 2012). At these lower masses, runaway O and Si burning triggered by the PI may not unbind the star. Its outer layers, which are weakly bound if it dies as a red supergiant, are ejected instead. We now examine this process in greater detail by considering the PPI SN from Woosley et al. (2007) as an example. The progenitor was a  $110 M_{\odot}$  solar-metallicity star whose evolution was modeled in the Kepler stellar evolution code (Weaver et al. 1978; Woosley et al. 2002). Mass loss was heavily suppressed over its lifetime to approximate the evolution of a Pop III star. At the onset of the PI the mass of the star is  $74.6 M_{\odot}$ , with a  $49.9 M_{\odot}$  He core. It dies as a red supergiant, with a radius of  $1.1 \times 10^{14}$  cm and a luminosity of  $9.2 \times 10^{39}$  erg  $s^{-1}$ .

Loss of thermal pressure support in the core due to the conversion of photons into  $e^+ - e^-$  pairs causes it to contract, radiate neutrinos and light, and grow in temperature from  $\sim 10^9$  K to  $3.04 \times 10^9$  K, well above the usual  $2.0 \times 10^9$  K at which O burns stably in massive stars. Explosive nuclear burning ensues, consuming  $1.49 M_{\odot}$  of O and  $1.55 M_{\odot}$  of C and releasing  $1.4 \times 10^{51}$  erg. Most of this energy goes into expanding the star but  $\sim 10\%$  is channeled into the expulsion of the weakly bound outer layers of the core and surrounding envelope ( $24.5 M_{\odot}$ , mostly He and some H). This first shell is ejected at velocities of  $100 - 1000$  km  $s^{-1}$ . As shown in Fig. 2 of

Woosley et al. (2007), the ejection of the envelope looks like a weak SN, with a brief breakout luminosity of  $10^{42.7}$  erg  $s^{-1}$  followed by a  $10^{41.9}$  erg  $s^{-1}$  plateau that is powered primarily by He recombination.

What remains after the initial outburst is a  $50.7 M_{\odot}$  star that is slightly more massive than the original He core. It again contracts, emits neutrinos and becomes hotter. After another 6.8 years the core again encounters the pair instability and ejects another shell into space. This shell is less massive,  $5.1 M_{\odot}$ , but more energetic,  $6.0 \times 10^{50}$  erg. It is soon followed by an even less massive but slightly faster shell that quickly overtakes it and collides with it, as shown in the left and right panels of Fig. 1. This initial collision is luminous but buried in an optically thick medium and would not be observed. Nine years later the core contracts a final time, entering a stable Si burning phase that produces an Fe core that later collapses. If the core is rapidly rotating it could create a gamma-ray burst, either by forming a rapidly-spinning neutron star (millesecond magnetars; e.g., Metzger et al. 2011) or a black hole accretion disk system (collapsars; e.g., MacFadyen & Woosley 1999). In this study we consider only the collision of the second two shells with the first and examine the NIR, radio and x-ray signatures of Pop III GRBs elsewhere (Whalen et al. 2008a; Mesler et al. 2012, 2013).

## 3. NUMERICAL MODELS

Light curves and spectra for PPI SNe are calculated in three stages. First, we map the Kepler blast profiles from Woosley et al. (2007) shown in the right panel of Fig. 1 into the RAGE code and evolve them out to 9 yr. We then post process our RAGE profiles with the SPECTRUM code to construct light curves and spectra. Finally, these spectra are convolved with filter response functions, cosmological redshifting and absorption by the neutral IGM at high  $z$  to obtain NIR light curves in the observer frame.

### 3.1. RAGE

We model the collision between the pair pulsations with the Los Alamos code RAGE (Radiation Adaptive Grid Eulerian; Gittings et al. 2008; Frey et al. 2013). RAGE is an adaptive mesh refinement (AMR) radiation hydrodynamics code with a second-order conservative Godunov hydro scheme and grey or multigroup flux-limited diffusion for modeling transport in one, two, or three dimensions (1D, 2D, or 3D). RAGE uses atomic opacities compiled from the Los Alamos OPLIB database<sup>7</sup>(Magee et al. 1995) and can evolve multimaterial flows with several types of equation of state. Our RAGE models include multispecies advection and 2-temperature (2T) radiation transport in which the matter and radiation temperatures, while coupled, are evolved separately. We also include the self-gravity of the ejected shells and the gravity due to the remnant star, which is treated as a point mass at the center of the coordinate mesh. We evolve mass fractions for 15 elements: H, He, C, N, O, Ne, Mg, Si, S, Ar, Ca, Ti, Cr, Fe and Ni.

#### 3.1.1. Model Setup

<sup>7</sup> <http://aphysics2/www.t4.lanl.gov/cgi-bin/opacity/tops.pl>

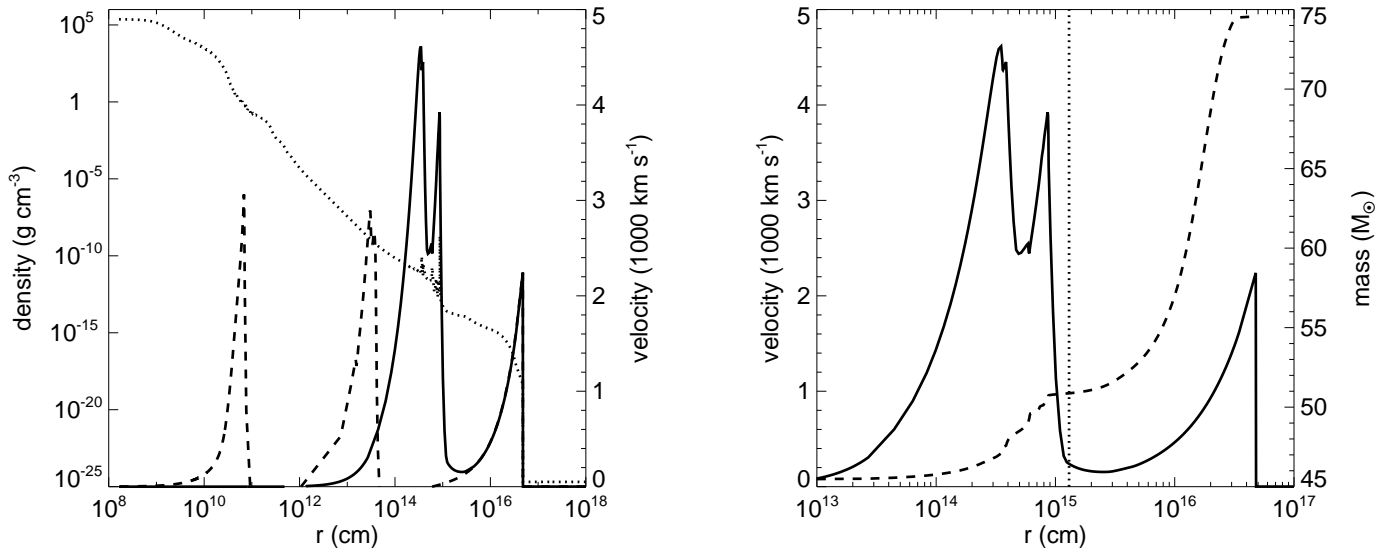


FIG. 1.— Evolution of the PPI. Left: density (dotted) and velocity (dashed) profiles for the star and its three pulsations just after the third ejection. The solid line is the velocity profile when the second and third pulses begin to overtake the first, about 120 d after the third pulse. Right: enlarged view of the collision of the second and third pulsations with the first. Solid line: velocities; dashed line: mass interior to the given radius; dotted: the boundary between the second two pulses and the first. This is the velocity profile that is initialized in RAGE.

Our 1D spherical coordinate root grid has 100,000 uniform zones with an initial resolution of  $1 \times 10^{11}$  cm and inner and outer boundaries at  $2.0 \times 10^{12}$  and  $1.0 \times 10^{16}$  cm, respectively. The inner boundary is chosen to excise the remnant star from the grid, whose high central densities and temperatures would restrict the solution to unnecessarily small Courant time steps. However, the gravity of this remnant, whose mass is  $45.5 M_{\odot}$  at the time the simulation is launched, is included in our model as a point mass at the inner boundary. Up to 4 levels of refinement are applied in the initial interpolation of the profiles onto the setup grid and then during the simulation. The grid is refined on the ratio of the second derivative to the first derivative in density, pressure and velocity according to the prescription of Löhner (1987).

The region from the outer surface of the first pulsation to the outer boundary of the grid is assumed to be a diffuse ( $n = 0.1 \text{ cm}^{-3}$ ) H II region with a temperature of 0.01 eV and mass fractions of 76% H and 24% He. This is consistent with the general belief that Pop III stars ionize their halos (e.g., Whalen et al. 2004). We set reflecting and outflow boundary conditions on the fluid and radiation flows at the inner and outer boundaries of the mesh, respectively. To speed up the simulation and accommodate the expansion of the shells we resize the grid by a factor of 2.5 every  $10^6$  time steps. The initial time step on which the new series evolves scales approximately as the ratio of the new and old zone sizes. We again allow up to 4 levels of refinement when mapping the flow to a new grid and throughout the run thereafter.

### 3.2. SPECTRUM

To calculate a spectrum from a RAGE profile we map its densities, temperatures, mass fractions and velocities onto a 2D grid in  $r$  and  $\mu = \cos \theta$  in the SPECTRUM code. SPECTRUM performs a direct sum of the luminosity of every fluid element in the discretized profile to compute the total flux escaping the ejecta along the line of sight at every wavelength. SPECTRUM, which is described in detail in Frey et al. (2013), includes Doppler shifts and time dilation due to the relativistic expansion of the ejecta. It also calculates intensities of emission lines and the attenuation of flux along the line of sight, capturing both limb darkening and absorption lines imprinted on the flux by intervening material in the ejecta and wind.

Gas densities, velocities, mass fractions and radiation temperatures are first extracted from every level of the AMR hierarchy in RAGE and sequentially ordered by radius into separate files, with one variable per file. Because of limitations on machine memory and time only a subset of these points are mapped onto the SPECTRUM grid. We then determine the position of the shock formed as the second two shells plow up the first, which is taken to be where the gas velocity rises above  $2.3 \times 10^8 \text{ cm s}^{-1}$ . This velocity is chosen so that the inward sweep will not be halted by the first shell, whose peak velocity is  $2.1 \times 10^8 \text{ cm s}^{-1}$ . Next, we find the radius of the  $\tau = 40$  surface by integrating the optical depth due to Thomson scattering in from the outer boundary, taking  $\kappa_{Th}$  to be 0.288 for the material from the outer boundary up to the shock between the shells (see Section 2.4 of Whalen et al. 2013f). This is the greatest depth from which radiation can escape from the collision between the pulsations.

The extracted fluid variables are then interpolated onto

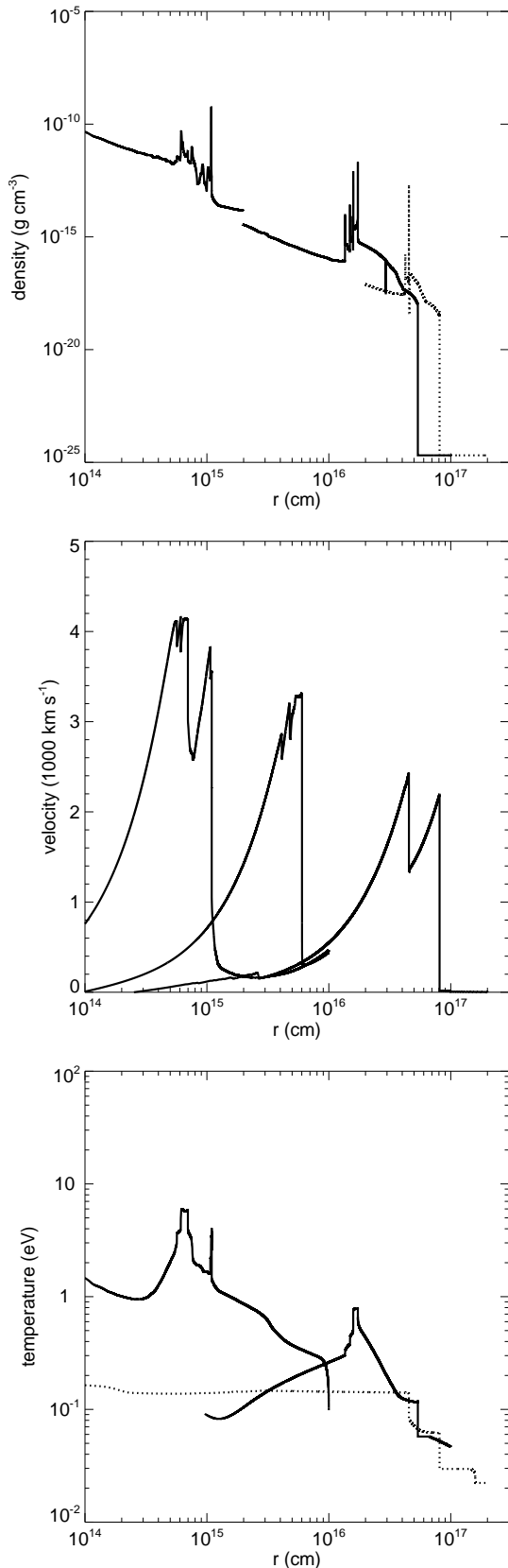


FIG. 2.— The collision between the second two pair pulsations and the first. Top: densities; center: velocities; bottom: temperatures. In the top panel, from left to right the times are 69 days, 1.6 yr, and 5.4 yr. In the bottom two panels, from left to right the times are 69 days, 5.1 months, and 5.4 yr.

the SPECTRUM grid as follows. The inner mesh boundary is the same as for the RAGE grid and the outer boundary is  $10^{18}$  cm. Eight hundred uniform zones in  $\log r$  are assigned from the center of the grid to the  $\tau = 40$  surface, and the region from the  $\tau = 40$  surface to the shock is partitioned into 6200 uniform zones in  $r$ . The region between the shock and the outer edge of the grid is divided into 500 uniform zones in  $\log r$  for a total of 7500 radial bins. The variables within each of these new radial bins are mass averaged so that the SPECTRUM grid captures very sharp features from the RAGE profile. The mesh is uniformly divided into 160 bins in  $\mu$  from -1 to 1. Our grid fully resolves regions of the collision from which photons can escape the flow and only lightly samples those from which they cannot.

#### 4. COLLISION PROFILES

Density, velocity and temperature profiles for the collision between the second two pair pulsations and the first are shown in Fig. 2. It is clear from the density profiles in Figs. 1 and 2 that the first shell is trailed by a relatively dense wind-like shroud that roughly has an  $r^{-2}$  profile but is basically stationary. As the second ejection plows through this envelope it rapidly decelerates and begins to shock the trailing edge of the first shell. The shocked gas piles up in a thin, hot dense layer at the leading edge of the second ejection. It is visible as the density spike at  $\sim 10^{15}$  cm at 69 days, at  $1.8 \times 10^{16}$  cm at 1.6 yr, and at  $4.0 \times 10^{16}$  cm at 5.4 yr. This thin layer is the origin of all the luminosity from the collision, which we show in the left panel of Fig. 3.

Unlike Type II<sub>n</sub> SNe, in which the collision between the ejecta and a shell are more abrupt, collisions between consecutive pair pulsations are more gradual because the first ejection has no distinct inner surface. Instead, the second ejection radiates more strongly as it becomes more mass loaded as it sweeps up the first shell. This is why the luminosity ramps up over a period of  $\sim 10$  days before reaching a maximum of  $\sim 7.0 \times 10^{43}$  erg  $s^{-1}$ . The collision radiates strongly for  $\sim 3$  yr as the relative kinetic energy of the shells is converted into heat and then light. Approximately 90% of the kinetic energy is radiated away as the second shell advances from  $10^{15}$  cm to  $2 \times 10^{16}$  cm. The rebrightening that is visible at  $\sim 600$  days is due to an abrupt pileup of gas in the shocked layer that is visible as the density spike at  $1.8 \times 10^{16}$  cm at 1.6 yr. This bump in luminosity peaks at  $\sim 10^{43}$  erg  $s^{-1}$  and lasts about 500 days.

The ripples in the bolometric luminosity, which are also manifest in the NIR light curves, are due to the classic radiative instability described by Chevalier & Imamura (1982) and Imamura et al. (1984). As the second two pulses plow up the first, a reverse shock forms, detaches from the forward shock, and backsteps into the flow in the frame of the forward shock. But if the postshock gas can radiatively cool, as this gas does, the reverse shock loses pressure support and recedes back toward the forward shock. As the forward shock plows up more material the cycle repeats. The fluctuations in overall luminosity are due to this cycle, and since the bolometric luminosity varies by up to 50% we infer that flux from the reverse shock is at times similar to that of the forward shock. The STELLA light curves from Woosley et al. (2007) also exhibit this radiative instability. In a multi-



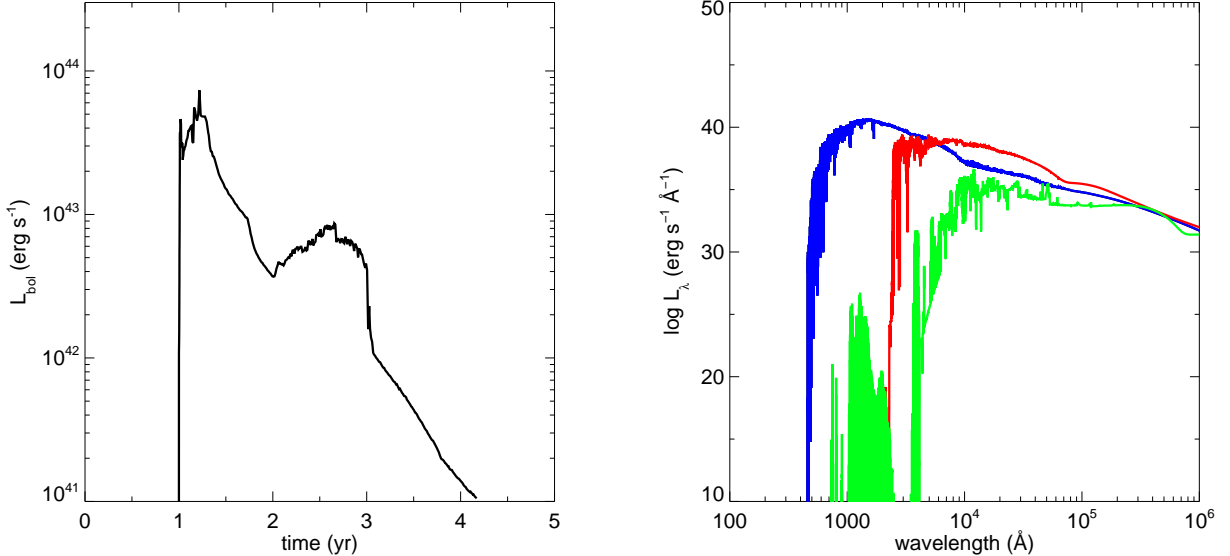


FIG. 3.— Left panel: bolometric luminosities for the pair pulsation collision. Right panel: spectra for the collision at 69 days (blue), 1.6 yr (red), and 5.4 yr (green).

dimensional simulation, the narrow region between the colliding shells in which the radiative instability occurs would likely be broken up by Rayleigh-Taylor (RT) instabilities, and this might reduce or remove altogether the fluctuations in the light curve. These instabilities would also disrupt the density structures emitting most of the radiation from the collision, and it is unclear how this would change the luminosity.

RAGE and STELLA yield similar bolometric luminosities early in the collision, but there are some differences. From 200 - 600 days the RAGE luminosities fall below  $10^{43}$  erg s $^{-1}$  before rebrightening, while the STELLA light curve falls more gradually. There are also features in the peak luminosities in RAGE that are distinct from those in STELLA. These discrepancies can be attributed to differences in resolution, atomic physics and hydrodynamic schemes, and opacities between the two codes. Differences between the opacities in OPLIB and in STELLA in particular could change photon diffusion times through the flow and the duration of the light curves. However, the two codes exhibit similar bolometric luminosities overall. The steeper decline in the RAGE light curve suggests that PPI SNe may be more easily detected at high  $z$  than STELLA might predict because of the greater variability after redshifting.

It might be thought that the PPI SN would not appear to be a transient at high redshift because its bolometric luminosity is relatively uniform for a year in the rest frame. This emission would last 10 - 20 yr for  $z = 10$  - 20 events in the observer frame. But the spectra evolve considerably over this time, as we show in the right panel of Fig. 3 and the temperatures in Fig. 1. At  $\sim 70$  days the shock is hottest,  $\sim 5$  eV or 55,000 K, and its spectrum cuts off at about 500 Å. At this stage the collision radiates strongly in the UV, like Type II $n$  SNe. As the collision proceeds and more of the relative kinetic energy of the shells is dissipated, the shock cools and its spectrum softens. At 1.6 yr, when the collision temporarily rebrightens, the shock has cooled to  $\sim 11,000$  K and its

spectrum cuts off at  $\sim 2000$  Å. By 5.4 yr the collision has cooled to  $\sim 1500$  K and its spectrum has evolved into the optical and IR. At this point the shells have become transparent and their photons have escaped into the IGM, as shown by the flat material temperatures in Fig. 2.

The PPI SN is similar to the Type II $n$  SNe studied by Whalen et al. (2013b) in that it is bright in the UV at early stages of the collision, when the shock has large radii,  $\sim 10^{15}$  cm. This radius is also similar to the inner radii of shells of the Type II $n$  events in Whalen et al. (2013b) when the ejecta crashes into them. With similar shock temperatures and radii upon collisions, the initial total luminosities for PPI SNe and Type II $n$  might be expected to be comparable, and inspection of Fig. 2 in Whalen et al. (2013b) confirms this to be the case. As the shock approaches radiation breakout from the first shell, one would expect low-energy photons to filter out first and later be followed by higher energy photons because opacities are generally greater at shorter wavelengths. But the temperature of the shock rises in the early stages of the collision so both processes harden the spectrum as radiation fully emerges from the shell.

We note that it is primarily bound-bound and bound-free emission from the shocked region between the second two shells and the first that comprises the spectrum. In our models, the collision does not produce temperatures that are high enough for bremsstrahlung x-rays, as might occur in more energetic events. The spectra are basically blackbody with emission and absorption lines from the shells. These latter features are prominent in the spectra at later times, which appear to be blackbody but are sheared off at short wavelengths.

Although our model does not produce x-rays, they might be emitted in real events by non local-thermodynamic-equilibrium (non-LTE) processes in the shock. If ions in the shocked region between the shells decouple from electrons at early times they could rise to higher temperatures than in our models because they cannot efficiently radiate away the heat deposited by the

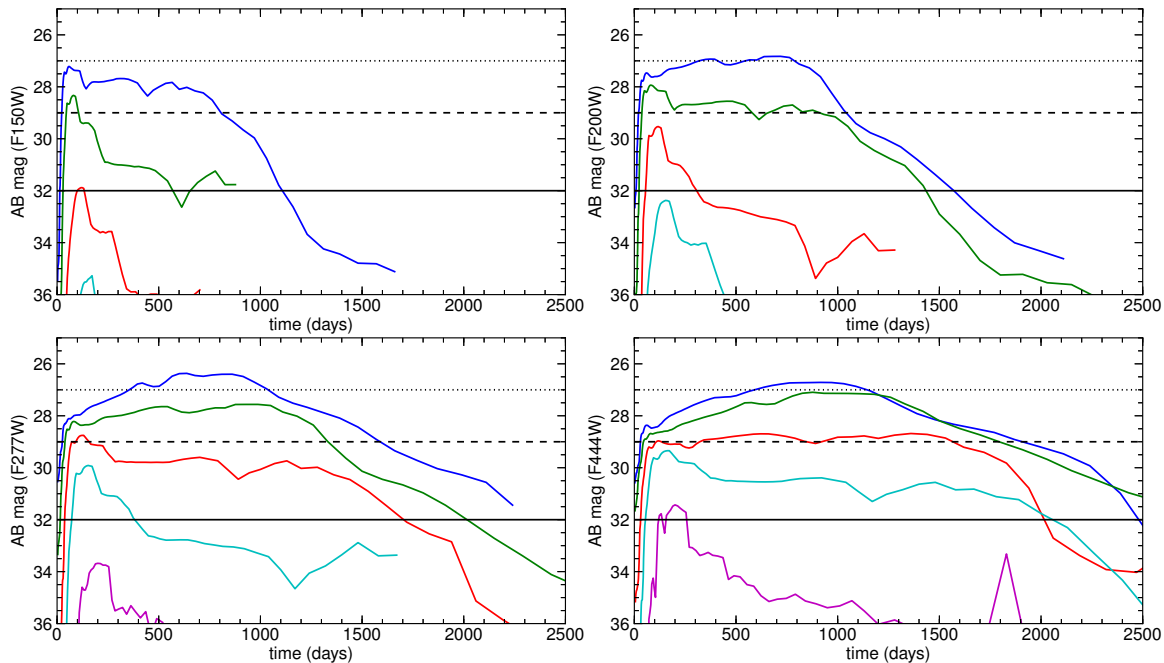


FIG. 4.— PPI SN NIR light curves at  $z = 7$  (blue), 10 (green), 15 (red), 20 (cyan) and 30 (purple). The horizontal lines are photometry limits for WFIRST (dotted), WFIRST with spectrum stacking (dashed), and *JWST* (solid).

shock. Under these circumstances the shock might emit x-rays at later times. Efforts are now underway to implement three-temperature (3T) physics in RAGE, in which ions, electrons, and photons are evolved at separate temperatures, to capture non-LTE processes. Although such x-rays would not be detected from high- $z$  explosions due to absorption by the neutral IGM, they might be visible in local events.

We also note that although the spectrum at times appears to be blackbody, one cannot fit a blackbody to the effective temperature of the shock to estimate the NIR flux from a high-redshift SN in lieu of an actual spectrum calculation. The UV that is redshifted into the NIR comes from the short wavelength limit of the spectrum, which, unlike the longer wavelengths, is poorly approximated by a blackbody because of absorption by the shells. A blackbody fit based on the lower wavelengths would overestimate flux at these short wavelengths and predict too much NIR luminosity today.

### 5. NIR LIGHT CURVES / DETECTION LIMITS

To obtain NIR light curves from the spectra, we first cosmologically redshift and dim them. They are then corrected for absorption by the neutral IGM at high redshift according to the prescription of Madau (1995). Several models for absorption by the neutral IGM exist in the literature but they yield similar transmission factors, as discussed by de Souza et al. (2013). We then convolve the spectra with filter response functions for *JWST* and WFIRST with the synthetic photometry code of Su et al. (2011) to compute NIR light curves.

We show light curves for the PPI SN in four *JWST* filters ( $1.5 \mu\text{m}$ ,  $2 \mu\text{m}$ ,  $2.77 \mu\text{m}$ , and  $4.44 \mu\text{m}$  at  $z = 7, 10, 15, 20$  and 30) in Fig. 4. The PPI SN is visible at  $z \gtrsim 30$  to *JWST*, whose photometry limit is AB mag 32. The light curves all exhibit rapid rise times that correspond to the breakout of radiation from the first shell.

Breakout is followed by a gradual rise in luminosity as the shock grows in radius. But this rise and later decline has fluctuations that are due to hydrodynamics. As the shock expands it runs into density structures that cause it to intermittently brighten. Fluctuations in densities and shock temperatures also result in variations in opacities in front of the shock. Such features are present in Type II<sub>n</sub> NIR light curves at early times as SN ejecta plows up density structures in the collision zone (see Fig. 10 in Whalen et al. 2013b).

The PPI SN shock is brighter but a little cooler than the Type II<sub>n</sub> collisions examined by Whalen et al. (2013b). At  $z = 15$ , the PPI SN is about two magnitudes brighter than the Type II<sub>n</sub>, but at  $4.44 \mu\text{m}$  rather than  $3.56 \mu\text{m}$ . The collision between the faster SN ejecta and the shell in Type II<sub>ne</sub> creates higher shock temperatures but happens at somewhat smaller radii, and is therefore less luminous. We note that the SN considered by Whalen et al. (2013b) only had an energy of  $2.4 \times 10^{51}$  erg and was therefore a conservative case. In many Type II<sub>ne</sub> the ejecta can have much more energy and the collision could be superluminous (e.g., SN 2006gy; Moriya et al. 2013) and nearly as bright in the NIR as a PPI SN at high redshift.

At  $z \gtrsim 15$  the PPI SN is slightly dimmer than the nominal detection limit of WFIRST at  $4 \mu\text{m}$ , AB mag 27. However, simple spectrum stacking could extend this limit down to 29. If so, WFIRST could detect these events out to  $z \sim 20$  at 2 - 4 times the rate of PPI SNe, or perhaps hundreds over its mission lifetime as discussed in Section 6 of Whalen et al. (2013a). The possibility of building up the Pop III IMF and tracing cosmic star formation rates at high redshift by detecting large numbers of primeval SNe underscores the need for all-sky NIR missions such as WFIRST and WISH.

We note that with only modest gravitational lensing that PPI SNe could be found in the *Cluster Lensing and*

*Supernova Survey with Hubble (CLASH)* at  $z \sim 7 - 12$  because the H band ( $1.63 \mu\text{m}$ ) photometry limit of the Wide-Field Camera 3 (WFC3) is  $\sim \text{AB mag } 27.3$ . However, it is not clear if there are enough PPI SN at this epoch to be enclosed by the volume that is lensed by the clusters in the survey. For the mean of the star formation rates (SFRs) discussed in the next section, Whalen et al. (2013i) find that up to a dozen SNe from  $5 < z < 12$  may already have been found by *CLASH*. For most IMFs it is unlikely that any of these events would be a PPI SN.

## 6. CONCLUSION

Pop III PPI SNe can be used to probe the primordial universe because they are visible at  $z \gtrsim 30$  to *JWST* and at  $z \gtrsim 20$  to *WFIRST*. They will complement PI SNe, Type II<sub>ne</sub> and supermassive Pop III SNe, which are visible out to similar redshifts. PPI SN light curves are easily distinguished from those of other Pop III SNe, and their variability over likely protogalactic survey times will clearly identify them as transients in future surveys. Besides revealing the properties of early stars, Pop III SNe will pinpoint the positions of ancient galaxies on the sky that otherwise might not have been discovered. They will also constrain star formation rates in the first galaxies, which will yield important clues about their evolution at early times.

Although we have considered a solar-mass progenitor as a proxy for a Pop III star, this will not have a large effect on the energetics of the PPI or the NIR light curve of the collision. The energetics of the central engine primarily depend on the entropy profile of the core of the star at the end of its life, which is similar for solar-metallicity and Pop III stars of equal mass (e.g., Chieffi & Limongi 2004; Woosley & Heger 2007) (see also Fig. 1 of Whalen & Fryer 2012). But metals could enhance cooling in the shocked gas between the shells and lead to denser and thinner structures with lower temperatures and luminosities. Metals also impose a more complex line structure on the spectra of the collision than would be present in zero-metallicity explosions. All of this, together with the somewhat larger opacity in the surrounding envelope due to the metals, suggests that the NIR luminosities in our simulation are a lower limit to those for Pop III events.

While our fiducial model demonstrates that PPI SNe will be visible out to  $z \sim 20$  in future observational campaigns, more work must be done to determine the range

of stellar masses for which PPI SNe can be detected at high redshift. Although Pop III stars from  $85 - 140 M_{\odot}$  can die in pulsational explosions, only those with He core masses from  $40 - 50 M_{\odot}$  will produce very luminous events because the timescales between their pulsations are short enough for the shells to actually collide (on the order of years). Also, for this range in mass the collisions occur at radii of  $\sim 10^{16}$  cm, where most of their energy is emitted in the UV and optical. As noted above, RT instabilities will induce mixing at the interface between the colliding shells and alter their luminosity. Future studies should be multidimensional, and focus on explosions in this mass range.

Detection rates for PPI SNe at high redshift hinge on the cosmic SFR. Current estimates of the cosmic SFR from GRBs (Ishida et al. 2011; Robertson & Ellis 2012), SNe (Cooke et al. 2012), early galaxies (Campisi et al. 2011) and simulations (Tornatore et al. 2007; Trenti & Stiavelli 2009; Wise et al. 2012; Johnson et al. 2013a; Pawlik et al. 2013; Xu et al. 2013; Hasegawa & Semelin 2013; Muratov et al. 2013) vary by more than two orders of magnitude above  $z \sim 10$  (see also Section 4 of Whalen et al. 2013i). Assuming fairly conservative SFRs, 5 - 10 Pop III PI SNe could be found by *JWST* over its lifetime (Hummel et al. 2012). Depending on the slope of the IMF, twice as many PPI SNe could be found. Wide-field campaigns by *WFIRST* and *WISH* might discover hundreds of these events.

We thank the anonymous referee, whose suggestions improved the quality of this paper. DJW acknowledges support from the Baden-Württemberg-Stiftung by contract research via the programme Internationale Spitzenforschung II (grant P-LS-SPII/18). JS and JLJ were supported by LANL LDRD Director's Fellowships. MS thanks Marcia Rieke for making available the NIRC<sub>am</sub> filter curves and was partially supported by NASA *JWST* grant NAG5-12458. At Santa Cruz, research was supported by NASA (NNX09AK36G) and the DOE-HEP Program (DE-SC0010676). Work at LANL was done under the auspices of the National Nuclear Security Administration of the U.S. Department of Energy at Los Alamos National Laboratory under Contract No. DE-AC52-06NA25396. All RAGE and SPECTRUM calculations were performed on Institutional Computing (IC) and Yellow network platforms at LANL (Pinto, Mustang and Moonlight).

## REFERENCES

- Abel, T., Bryan, G. L., & Norman, M. L. 2002, *Science*, 295, 93  
 Abel, T., Wise, J. H., & Bryan, G. L. 2007, *ApJ*, 659, L87  
 Agarwal, B., Khochfar, S., Johnson, J. L., Neistein, E., Dalla Vecchia, C., & Livio, M. 2012, *MNRAS*, 425, 2854  
 Alvarez, M. A., Bromm, V., & Shapiro, P. R. 2006, *ApJ*, 639, 621  
 Alvarez, M. A., Wise, J. H., & Abel, T. 2009, *ApJ*, 701, L133  
 Beers, T. C. & Christlieb, N. 2005, *ARA&A*, 43, 531  
 Bromm, V., Coppi, P. S., & Larson, R. B. 2002, *ApJ*, 564, 23  
 Bromm, V. & Loeb, A. 2003, *ApJ*, 596, 34  
 Caffau, E., Bonifacio, P., François, P., Spite, M., Spite, F., Zaggia, S., Ludwig, H.-G., Steffen, M., Mashonkina, L., Monaco, L., Sbordone, L., Molaro, P., Cayrel, R., Plez, B., Hill, V., Hammer, F., & Randich, S. 2012, *A&A*, 542, A51  
 Campisi, M. A., Maio, U., Salvaterra, R., & Ciardi, B. 2011, *MNRAS*, 416, 2760  
 Cayrel, R., Depagne, E., Spite, M., Hill, V., Spite, F., François, P., Plez, B., Beers, T., Primas, F., Andersen, J., Barbuy, B., Bonifacio, P., Molaro, P., & Nordström, B. 2004, *A&A*, 416, 1117  
 Chatzopoulos, E. & Wheeler, J. C. 2012, *ApJ*, 748, 42  
 Chevalier, R. A. & Imamura, J. N. 1982, *ApJ*, 261, 543  
 Chiaki, G., Yoshida, N., & Kitayama, T. 2013, *ApJ*, 762, 50  
 Chieffi, A. & Limongi, M. 2004, *ApJ*, 608, 405  
 Choi, J.-H., Shlosman, I., & Begelman, M. C. 2013, *ApJ*, 774, 149  
 Clark, P. C., Glover, S. C. O., Smith, R. J., Greif, T. H., Klessen, R. S., & Bromm, V. 2011, *Science*, 331, 1040  
 Cooke, J., Sullivan, M., Gal-Yam, A., Barton, E. J., Carlberg, R. G., Ryan-Weber, E. V., Horst, C., Omori, Y., & Diaz, C. G. 2012, *Nature*, 491, 228

- de Souza, R. S., Ishida, E. E. O., Johnson, J. L., Whalen, D. J., & Mesinger, A. 2013, *MNRAS*, 436, 1555
- Dessart, L., Waldman, R., Livne, E., Hillier, D. J., & Blondin, S. 2013, *MNRAS*, 428, 3227
- Djorgovski, S. G., Volonteri, M., Springel, V., Bromm, V., & Meylan, G. 2008, in *The Eleventh Marcel Grossmann Meeting On Recent Developments in Theoretical and Experimental General Relativity, Gravitation and Relativistic Field Theories*, ed. H. Kleinert, R. T. Jantzen, & R. Ruffini, 340–367
- Febel, A., Aoki, W., Christlieb, N., Ando, H., Asplund, M., Barklem, P. S., Beers, T. C., Eriksson, K., Fechner, C., Fujimoto, M. Y., Honda, S., Kajino, T., Minezaki, T., Nomoto, K., Norris, J. E., Ryan, S. G., Takada-Hidai, M., Tsangarides, S., & Yoshii, Y. 2005, *Nature*, 434, 871
- Frey, L. H., Even, W., Whalen, D. J., Fryer, C. L., Hungerford, A. L., Fontes, C. J., & Colgan, J. 2013, *ApJS*, 204, 16
- Fryer, C. L., Whalen, D. J., & Frey, L. 2010, in *American Institute of Physics Conference Series*, Vol. 1294, American Institute of Physics Conference Series, ed. D. J. Whalen, V. Bromm, & N. Yoshida, 70–75
- Gal-Yam, A., Mazzali, P., Ofek, E. O., Nugent, P. E., Kulkarni, S. R., Kasliwal, M. M., Quimby, R. M., Filippenko, A. V., Cenko, S. B., Chornock, R., Waldman, R., Kasen, D., Sullivan, M., Beshore, E. C., Drake, A. J., Thomas, R. C., Bloom, J. S., Poznanski, D., Miller, A. A., Foley, R. J., Silverman, J. M., Arcavi, I., Ellis, R. S., & Deng, J. 2009, *Nature*, 462, 624
- Gardner, J. P., Mather, J. C., Clampin, M., Doyon, R., Greenhouse, M. A., Hammel, H. B., Hutchings, J. B., Jakobsen, P., Lilly, S. J., Long, K. S., Lunine, J. I., McCaughrean, M. J., Mountain, M., Nella, J., Rieke, G. H., Rieke, M. J., Rix, H.-W., Smith, E. P., Sonneborn, G., Stiavelli, M., Stockman, H. S., Windhorst, R. A., & Wright, G. S. 2006, *Space Sci. Rev.*, 123, 485
- Gittings, M., Weaver, R., Clover, M., Betlach, T., Byrne, N., Coker, R., Dendy, E., Hueckstaedt, R., New, K., Oakes, W. R., Ranta, D., & Stefan, R. 2008, *Computational Science and Discovery*, 1, 015005
- Glover, S. 2013, in *Astrophysics and Space Science Library*, Vol. 396, *Astrophysics and Space Science Library*, ed. T. Wiklund, B. Mobasher, & V. Bromm, 103
- Greif, T. H., Bromm, V., Clark, P. C., Glover, S. C. O., Smith, R. J., Klessen, R. S., Yoshida, N., & Springel, V. 2012, *MNRAS*, 424, 399
- Greif, T. H., Glover, S. C. O., Bromm, V., & Klessen, R. S. 2010, *ApJ*, 716, 510
- Greif, T. H., Johnson, J. L., Klessen, R. S., & Bromm, V. 2008, *MNRAS*, 387, 1021
- Greif, T. H., Springel, V., White, S. D. M., Glover, S. C. O., Clark, P. C., Smith, R. J., Klessen, R. S., & Bromm, V. 2011, *ApJ*, 737, 75
- Hasegawa, K. & Semelin, B. 2013, *MNRAS*, 428, 154
- Heger, A. & Woosley, S. E. 2002, *ApJ*, 567, 532
- Hirano, S., Hosokawa, T., Yoshida, N., Umeda, H., Omukai, K., Chiaki, G., & Yorke, H. W. 2013, *arXiv:1308.4456*
- Hosokawa, T., Omukai, K., Yoshida, N., & Yorke, H. W. 2011, *Science*, 334, 1250
- Hosokawa, T., Yoshida, N., Omukai, K., & Yorke, H. W. 2012, *ApJ*, 760, L37
- Hummel, J. A., Pawlik, A. H., Milosavljević, M., & Bromm, V. 2012, *ApJ*, 755, 72
- Imamura, J. N., Wolff, M. T., & Durisen, R. H. 1984, *ApJ*, 276, 667
- Ishida, E. E. O., de Souza, R. S., & Ferrara, A. 2011, *MNRAS*, 418, 500
- Jeon, M., Pawlik, A. H., Greif, T. H., Glover, S. C. O., Bromm, V., Milosavljević, M., & Klessen, R. S. 2012, *ApJ*, 754, 34
- Joggerst, C. C., Almgren, A., Bell, J., Heger, A., Whalen, D., & Woosley, S. E. 2010, *ApJ*, 709, 11
- Joggerst, C. C. & Whalen, D. J. 2011, *ApJ*, 728, 129
- Johnson, J. L. & Bromm, V. 2007, *MNRAS*, 374, 1557
- Johnson, J. L., Dalla, V. C., & Khochfar, S. 2013a, *MNRAS*, 428, 1857
- Johnson, J. L., Greif, T. H., & Bromm, V. 2008, *MNRAS*, 388, 26
- Johnson, J. L., Greif, T. H., Bromm, V., Klessen, R. S., & Ippolito, J. 2009, *MNRAS*, 399, 37
- Johnson, J. L., Whalen, D. J., Even, W., Fryer, C. L., Heger, A., Smidt, J., & Chen, K.-J. 2013b, *arXiv:1304.4601*
- Johnson, J. L., Whalen, D. J., Fryer, C. L., & Li, H. 2012, *ApJ*, 750, 66
- Johnson, J. L., Whalen, D. J., Li, H., & Holz, D. E. 2013c, *ApJ*, 771, 116
- Kasen, D., Woosley, S. E., & Heger, A. 2011, *ApJ*, 734, 102
- Kitayama, T., Yoshida, N., Susa, H., & Umemura, M. 2004, *ApJ*, 613, 631
- Lai, D. K., Bolte, M., Johnson, J. A., Lucatello, S., Heger, A., & Woosley, S. E. 2008, *ApJ*, 681, 1524
- Latif, M. A., Schleicher, D. R. G., Schmidt, W., & Niemeyer, J. 2013a, *MNRAS*, 433, 1607
- 2013b, *MNRAS*, 430, 588
- Leloudas, G., Chatzopoulos, E., Dilday, B., Gorosabel, J., Vinko, J., Gallazzi, A., Wheeler, J. C., Bassett, B., Fischer, J. A., Frieman, J. A., Fynbo, J. P. U., Goobar, A., Jelínek, M., Malesani, D., Nichol, R. C., Nordin, J., Östman, L., Sako, M., Schneider, D. P., Smith, M., Sollerman, J., Stritzinger, M. D., Thöne, C. C., & de Ugarte Postigo, A. 2012, *A&A*, 541, A129
- Lippai, Z., Frei, Z., & Haiman, Z. 2009, *ApJ*, 701, 360
- Löhner, R. 1987, *Comput. Methods Appl. Mech. Eng.*, 61, 323
- MacFadyen, A. I. & Woosley, S. E. 1999, *ApJ*, 524, 262
- Mackey, J., Bromm, V., & Hernquist, L. 2003, *ApJ*, 586, 1
- Madau, P. 1995, *ApJ*, 441, 18
- Magee, N. H., Abdallah, Jr., J., Clark, R. E. H., Cohen, J. S., Collins, L. A., Csanak, G., Fontes, C. J., Gauger, A., Keady, J. J., Kilcrease, D. P., & Merts, A. L. 1995, in *Astronomical Society of the Pacific Conference Series*, Vol. 78, *Astrophysical Applications of Powerful New Databases*, ed. S. J. Adelman & W. L. Wiese, 51
- Margutti, R., Milosavljević, D., Soderberg, A. M., Chornock, R., Zauderer, B. A., Murase, K., Guidorzi, C., Sanders, N. E., Kuin, P., Fransson, C., Levesque, E. M., Chandra, P., Berger, E., Bianco, F. B., Brown, P. J., Challis, P., Chatzopoulos, E., Cheung, C. C., Choi, C., Chomiuk, L., Chugai, N., Contreras, C., Drout, M. R., Fesen, R., Foley, R. J., Fong, W., Friedman, A. S., Gall, C., Gehrels, N., Hjorth, J., Hsiao, E., Kirshner, R., Im, M., Leloudas, G., Lunnan, R., Marion, G. H., Martin, J., Morrell, N., Neugent, K. F., Omodei, N., Phillips, M. M., Rest, A., Silverman, J. M., Strader, J., Stritzinger, M. D., Szalai, T., Utterback, N. B., Vinko, J., Wheeler, J. C., Arnett, D., Campana, S., Chevalier, R., Ginsburg, A., Kamble, A., Roming, P. W. A., Pritchard, T., & Stringfellow, G. 2013, *arXiv:1306.0038*
- Mesler, R. A., Whalen, D. J., Lloyd-Ronning, N. M., Fryer, C. L., & Pihlström, Y. M. 2012, *ApJ*, 757, 117
- 2013, *ApJ*, in prep
- Metzger, B. D., Giannios, D., Thompson, T. A., Bucciantini, N., & Quataert, E. 2011, *MNRAS*, 413, 2031
- Milosavljević, M., Bromm, V., Couch, S. M., & Oh, S. P. 2009, *ApJ*, 698, 766
- Moriya, T. J., Blinnikov, S. I., Tominaga, N., Yoshida, N., Tanaka, M., Maeda, K., & Nomoto, K. 2013, *MNRAS*, 428, 1020
- Muratov, A. L., Gnedin, O. Y., Gnedin, N. Y., & Zemp, M. 2013, *ApJ*, 773, 19
- Nakamura, F. & Umemura, M. 2001, *ApJ*, 548, 19
- Pan, T., Kasen, D., & Loeb, A. 2012, *MNRAS*, 422, 2701
- Park, K. & Ricotti, M. 2011, *ApJ*, 739, 2
- 2012, *ApJ*, 747, 9
- 2013, *ApJ*, 767, 163
- Pawlik, A. H., Milosavljević, M., & Bromm, V. 2011, *ApJ*, 731, 54
- 2013, *ApJ*, 767, 59
- Reisswig, C., Ott, C. D., Abdikamalov, E., Haas, R., Moesta, P., & Schnetter, E. 2013, *arXiv:1304.7787*
- Ritter, J. S., Safrank-Shrader, C., Gnat, O., Milosavljević, M., & Bromm, V. 2012, *ApJ*, 761, 56
- Robertson, B. E. & Ellis, R. S. 2012, *ApJ*, 744, 95
- Rydberg, C.-E., Zackrisson, E., Lundqvist, P., & Scott, P. 2013, *MNRAS*, 429, 3658
- Safrank-Shrader, C., Milosavljević, M., & Bromm, V. 2013, *arXiv:1307.1982*
- Scannapieco, E., Madau, P., Woosley, S., Heger, A., & Ferrara, A. 2005, *ApJ*, 633, 1031
- Schleicher, D. R. G., Palla, F., Ferrara, A., Galli, D., & Latif, M. 2013, *arXiv:1305.5923*
- Smith, B. D. & Sigurdsson, S. 2007, *ApJ*, 661, L5



- Smith, B. D., Turk, M. J., Sigurdsson, S., O'Shea, B. W., & Norman, M. L. 2009, *ApJ*, 691, 441
- Smith, N., Mauerhan, J., & Prieto, J. 2013, arXiv:1308.0112
- Smith, N. & McCray, R. 2007, *ApJ*, 671, L17
- Smith, R. J., Glover, S. C. O., Clark, P. C., Greif, T., & Klessen, R. S. 2011, *MNRAS*, 414, 3633
- Stacy, A., Greif, T. H., & Bromm, V. 2010, *MNRAS*, 403, 45
- , 2012, *MNRAS*, 422, 290
- Su, J., Stiavelli, M., Oesch, P., Trenti, M., Bergeron, E., Bradley, L., Carollo, M., Dahlen, T., Ferguson, H. C., Giavalisco, M., Koekemoer, A., Lilly, S., Lucas, R. A., Mobasher, B., Panagia, N., & Pavlovsky, C. 2011, *ApJ*, 738, 123
- Susa, H. 2013, *ApJ*, 773, 185
- Tanaka, M., Moriya, T. J., & Yoshida, N. 2013, arXiv:1306.3743
- Tanaka, M., Moriya, T. J., Yoshida, N., & Nomoto, K. 2012, *MNRAS*, 422, 2675
- Tanaka, T. & Haiman, Z. 2009, *ApJ*, 696, 1798
- Tominaga, N., Morokuma, T., Blinnikov, S. I., Baklanov, P., Sorokina, E. I., & Nomoto, K. 2011, *ApJS*, 193, 20
- Tornatore, L., Ferrara, A., & Schneider, R. 2007, *MNRAS*, 382, 945
- Trenti, M. & Stiavelli, M. 2009, *ApJ*, 694, 879
- Turk, M. J., Abel, T., & O'Shea, B. 2009, *Science*, 325, 601
- Volonteri, M. 2012, *Science*, 337, 544
- Weaver, T. A., Zimmerman, G. B., & Woosley, S. E. 1978, *ApJ*, 225, 1021
- Whalen, D., Abel, T., & Norman, M. L. 2004, *ApJ*, 610, 14
- Whalen, D., O'Shea, B. W., Smidt, J., & Norman, M. L. 2008a, *ApJ*, 679, 925
- Whalen, D., van Veelen, B., O'Shea, B. W., & Norman, M. L. 2008b, *ApJ*, 682, 49
- Whalen, D. J. 2012, arXiv:1209.4688
- Whalen, D. J., Even, W., Frey, L. H., Smidt, J., Johnson, J. L., Lovekin, C. C., Fryer, C. L., Stiavelli, M., Holz, D. E., Heger, A., Woosley, S. E., & Hungerford, A. L. 2013a, *ApJ*, 777, 110
- Whalen, D. J., Even, W., Lovekin, C. C., Fryer, C. L., Stiavelli, M., Roming, P. W. A., Cooke, J., Pritchard, T. A., Holz, D. E., & Knight, C. 2013b, *ApJ*, 768, 195
- Whalen, D. J., Even, W., Smidt, J., Heger, A., Chen, K.-J., Fryer, C. L., Stiavelli, M., Xu, H., & Joggerst, C. C. 2013c, *ApJ*, 778, 17
- Whalen, D. J., Even, W., Smidt, J., Heger, A., Hirschi, R., Yusof, N., Stiavelli, M., Fryer, C. L., Chen, K.-J., & Joggerst, C. C. 2013d, arXiv:1312.5360
- Whalen, D. J. & Fryer, C. L. 2012, *ApJ*, 756, L19
- Whalen, D. J., Fryer, C. L., Holz, D. E., Heger, A., Woosley, S. E., Stiavelli, M., Even, W., & Frey, L. H. 2013e, *ApJ*, 762, L6
- Whalen, D. J., Joggerst, C. C., Fryer, C. L., Stiavelli, M., Heger, A., & Holz, D. E. 2013f, *ApJ*, 768, 95
- Whalen, D. J., Johnson, J. L., Smidt, J., Heger, A., Even, W., & Fryer, C. L. 2013g, *ApJ*, 777, 99
- Whalen, D. J., Johnson, J. L., Smidt, J., Meiksin, A., Heger, A., Even, W., & Fryer, C. L. 2013h, *ApJ*, 774, 64
- Whalen, D. J., Smidt, J., Johnson, J. L., Holz, D. E., Stiavelli, M., & Fryer, C. L. 2013i, arXiv:1312.6330
- Wise, J. H. & Abel, T. 2008, *ApJ*, 684, 1
- Wise, J. H., Turk, M. J., Norman, M. L., & Abel, T. 2012, *ApJ*, 745, 50
- Woosley, S. E., Blinnikov, S., & Heger, A. 2007, *Nature*, 450, 390
- Woosley, S. E. & Heger, A. 2007, *Phys. Rep.*, 442, 269
- Woosley, S. E., Heger, A., & Weaver, T. A. 2002, *Reviews of Modern Physics*, 74, 1015
- Xu, H., Wise, J. H., & Norman, M. L. 2013, *ApJ*, 773, 83